Journal Name

ARTICLE

Nanocomposites with BaTiO₃/SrTiO₃ hybrid fillers exhibiting enhanced dielectric behaviours and energy-storage densities

Dan Yu[a], Nuo-xin Xu[a], Liang Hu[a], Qi-long Zhang[*a] and Hui Yang[a, b]

Here, small loading of SrTiO₃ nanowires (ST NWs) were synthesized and grafted onto the surface of BaTiO₃ nanoparticles (BT NPs) in a hydrothermal process. Nanocomposites comprised of P(VDF-HFP) matrix and ceramic fillers were prepared using BT/ST nanocrystals of different molar ratios. Microstructure and thermal analysis confirm that BT NPs have been successfully functionalized with polyphenol-Sr²⁺ shells on the surface and the BT/ST-P(VDF-HFP) nanocomposites can obtain higher thermal stability than both pure P(VDF-HFP) and BT-P(VDF-HFP) composites. Dielectric properties measured at various frequencies and temperatures indicate that the nanocomposites with several BT/ST ratios exhibit enhanced dielectric properties over a wide frequency range. With a BT/ST molar ratio of 2, the dielectric constant of 7.5 vol% sample can increase by 3.2 and dielectric loss decrease by 0.015, compared with BT-P(VDF-HFP) nanocomposites. Besides the dielectric behaviours progress, the BT/ST-P(VDF-HFP) composites also possess higher electrical displacement and corresponding energy-storage densities than BT- P(VDF-HFP). The energy density of the optimal BT/ST-P(VDF-HFP) sample is four times more than that of pure P(VDF-HFP) under 20 kV/mm. All the improved performance suggests an easy method to fabricate nanocomposites bearing potential electrical applications.

Introduction

Polymer-ceramics nanocomposites are one of the most promising polymer nanocomposites so far, since this system can combine the desirable properties of both polymers and ceramics (i.e., high electric breakdown field strength and easy processing of polymers, high dielectric constant of ceramics) to obtain excellent dielectric performance.[1-4] Nanoparticles (NPs) are the most commonly used fillers, but a high volume fraction of NPs is required to achieve a high dielectric constant, meanwhile leading to an increase of dielectric loss and decline of breakdown strength.[5] In light of the vital role of the polymer/nanoparticle interfaces, many efforts have been devoted to improve the interfacial adhesion, and modifying NPs with organic surfactants or coupling agents is the commonly used method.[6,7] For example, Kim et al. functionalized BaTiO₃ NPs with fluoro-phosphonic acid ligand to reduce its surface energy and to obtain good dispersion in polymer matrix. And Zhu et al. indicated that the polymer shells outside BaTiO₃ NPs can influence the electrical properties and breakdown strength of the nanocomposites.[8,9] Nevertheless, the large gap in dielectric constant between fillers and matrix cannot be easily

solved, and surface modification cannot contribute remarkably to the electrical properties of the nanocomposites as well. Designing core-shell structured NPs is also a promising strategy to obtain high performance nanocomposites and various methods like in situ polymerization of monomers have been used to obtain NPs encapsulated with different shells.[10] Xie et al. have prepared core-shell structured BaTiO₃/poly(methyl methacrylate) nanocomposites and the effective k can be tailored by changing shell thickness.[11]

Besides the size and surface activity of fillers, shape also plays a pivotal role in the dielectric properties of composites since various shapes can lead to different interfacial polarization.[12] With higher aspect ratios and lower surface area, one-dimensional nanostructures like nanowires, nanofibers and nanorods are more effective in enhancing the properties of nanocomposites at low concentrations.[13] But dispersion difficulty and corresponding agglomeration of NWs are inevitable defects, especially at large loadings.

Due to the high dielectric constant, BaTiO₃ NPs have been used to prepare the 0-3 type nanocomposites in extended researches. However, the inhomogeneous electric field distribution and large remnant polarization in ferroelectric

BaTiO$_3$ can worsen the discharge efficiency of final composites.[14,15] And improvement of dielectric properties is always accompanied by degradation of the breakdown strength, especially at high volume fraction.[16] Compared with its counterpart, cubic-perovskite SrTiO$_3$ possesses a similar high dielectric constant and a lower dielectric loss; meanwhile, the stable paraelectric state at room temperature and above is favourable in reducing the remnant polarization.[17-19] Previous research has demonstrated the decreased surface energy of NWs, benefited from low surface area, can facilitate their homogeneous distribution while preventing agglomeration in the composites.[20,21] But the strategy of combining advantages of multiphase while using NW networks to improve the interfacial adhesion has seldom been reported in the open literature.

In this study, BaTiO$_3$ NPs and SrTiO$_3$ NWs are used as hybrid fillers to prepare P(VDF-HFP)-based nanocomposites. Small amount of SrTiO$_3$ NWs are grafted onto the BaTiO$_3$ surface via one-step hydrothermal process. The microstructure, thermal stability, surface morphology of as-synthesized ceramic fillers as well as the nanocomposites are investigated systematically. Additionally, the dielectric properties and energy storage capabilities of nanocomposites are also presented. The results not only indicate that the prepared nanocomposites can exhibit higher dielectric constant and energy storage densities compared with pure P(VDF-HFP), but also provide a flexible, green method to develop nanocomposites with hybrid ceramic fillers.

Experimental

Tetrabutyl titanate (TBT), strontium nitrate (Sr(NO$_3$)$_2$), tannic acid (TA), Tris(hydroxymethyl) aminomethane hydrochloride (Tris-HCl, AR), N, N-dimethyl formamide (DMF) and potassium hydroxide (KOH) were all purchased from Aladdin, China. Other principal materials include BaTiO$_3$ NPs (50-70 nm, Alfa Aesar) and Poly(vinylidene fluoride-co-hexafluoropylene) (P(VDF-HFP), pellets, Sigma-Aldrich). The typical procedure mainly contains two parts and here we take the BT/ST=2/1 sample as an example to illustrate it: For the functionalization of NPs, 1.72 mmol BT were first dispersed in 35 ml ultrapure water under vigorous stirring, then Sr(NO$_3$)$_2$ was added into the suspension and stirred for 3 h. After that, 0.86 mmol TA was slowly added into the suspension, and 5 ml Tris-HCl buffer solution (PH=9) was added 30 minutes later to promote the chelation. The mixture was washed, centrifuged and dried after stirring for 4 h. For the synthesis of NWs, functionalized BT NPs and KOH pellets were dissolved in water under stirring respectively, and then 0.86 mmol TBT was added into the KOH solution slowly to form white suspension. After stirring for another 3 h, the white suspension was dropped into the BT solution and mixed evenly. With 8 M KOH pellets added as the mineralizer, the mixed suspension was then poured into a stainless steel Teflon-lined autoclave and subjected to hydrothermal treatment under auto-generated pressure at 180 °C for 6 h. The resultant products were then washed,

centrifuged and dried at 60 °C for 12 h for subsequent preparation.

For the preparation of nanocomposites, P(VDF-HFP) was first dissolved in DMF and stirred for 6 h at room temperature. Then the functionalized nanopowders were dispersed into DMF slowly by ultra-sonication at room temperature for 1 h. After stirring for 12 h, the thin films were deposited by casting the as-synthesized mixture onto a glass substrate and heated in a vacuum oven at 60 °C for 4 h to remove the residual solvent. Finally, the dried nanocomposites were molded by hot-pressing at 200 °C under a pressure of about 2500 psi.

Characterization

Thermogravimetric analysis (TGA) was conducted on a TA-Q500 instrument at a heating rate of 10 °C·min^{-1} in the temperature range from 100 °C to 800 °C under a nitrogen flow. Differential scanning calorimetry (DSC) was performed using a TA-Q200 analyzer between 80 °C and 200 °C with a heating rate of 10 °C·min^{-1} under a nitrogen atmosphere. The IR Transmittance Spectra were collected by a FTIR spectrometer (Nicolet 5700, Thermo Fisher, USA) over the range of 600-4000 cm^{-1}. The phase composition of nanopowders was identified by powder X-ray diffraction (XRD, EMPYREAN, PANalytical Co., Netherlands) analysis, using Cu $K\alpha$ radiation in the 2θ range of 10°- 90°. Transmission electron microscopy (TEM) images were obtained from a CM 200UT instrument operated at an accelerating voltage of 200 kV. X-ray photoelectron spectroscopy (XPS) was recorded using an ESCALAB 250XI X-ray photoelectron spectrometer (Thermo Fisher Scientific, USA). The cross section morphology of the nanocomposites was characterized on a SU-70 field emission scanning electron microscope (SEM) instrument with all samples fractured in the liquid-nitrogen before testing.

Dielectric properties of the nanocomposites were performed on a broadband dielectric spectrometer (NOVOCONTROL GmbH, Germany) with Cu electrodes fabricating on both surfaces of the films. All the measurements were carried out in the frequency range of 10^{-1} to 10^7 Hz at several temperatures between 10 °C and 70 °C. The electric breakdown strength of the nanocomposites was measured by a dielectric breakdown tester at room temperature (CS2671A, China). Electric displacement-electric field (*D-E*) loops were measured on a PREMIER II-100V Ferroelectric material tester (Radiant Inc., USA) at room temperature using the same samples prepared for dielectric property testing. The polarization data were collected at different electric fields with a frequency of 100 Hz.

Results and discussion

Fig. 1 shows the morphology of the functionalized BT NPs and the BT/ST composites. Compared with the original NPs shown in Fig.1 (a), a light-contrast shell was introduced and coated neatly onto the surface of BT NPs via chelation. The dark field STEM image of BT-Sr^{2+} NPs in Fig. 1 (b) and element mapping in Fig. 1 (c) clearly indicate that the shell is a TA-Sr^{2+}

amorphous layer. It is noticed that the mapping signals of Sr^{2+} are a little weaker than those of Ba^{2+} and Ti^{4+}, which can be explained by the much thinner and amorphous shells. During functionalization of BT NPs, the galloyl groups of TA can
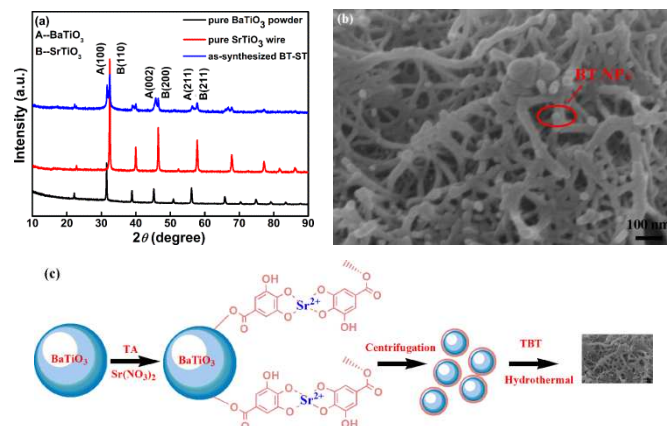
nanocrystals, in which TA can act as an organic ligand to chelate Sr^{2+} ions to form a stable, cross-linked TA-Sr^{2+} supramolecular shell. Therefore, the shells can be easily coated onto the surface of BT NPs due to their perfect surface binding
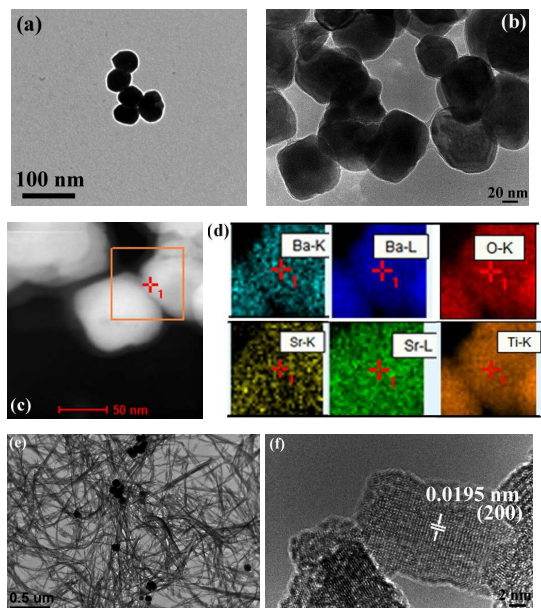
Fig. 1 TEM images of the BT-Sr^{2+} NPs and as-synthesized NWs: (a) original BT NPs (b) functionalized BT NPs (c) dark field STEM of BT-Sr^{2+} NPs (d) elemental mapping of BT-Sr^{2+} NPs. (e) NPs grafted with $SrTiO_3$ NWs (BT/ST=1/1). (f) HRTEM image of a single nanowire


Fig. 2 (a) XRD patterns of the original BT NPs, pure ST NWs and as-synthesized BT/ST compounds (BT/ST=2/1) (b) SEM image of the as-synthesized BT/ST compounds (c) Schematic illustration of the preparation process for the BT/ST nanocrystals

coordinate Sr^{2+} ions and form an octahedral complex,[22] in which Sr^{2+} can be trapped in the organic network stably. The functionalized BT NPs then acted as precursors in the hydrothermal reaction upon which cross-linked ST NWs can be synthesized. Fig. 1 (e) also displays the as-synthesized hybrid nanocrystals in which BT NPs are dispersed relatively homogenous in the network of ST NWs and the HRTEM image in Fig. 1 (f) of an individual nanowire also indicates good crystallinity of the synthesized ST NWs. The lattice fringe measured to be 0.0195 nm corresponds well with the (200) lattice spacing of cubic $SrTiO_3$ phase.

To further confirm the composition of the samples, Fig. 2 (a) presents the XRD patterns of original BT NPs and resulting BT/ST composites (BT/ST=2/1), and the XRD pattern of pure ST NWs synthesized under the same hydrothermal condition is also displayed as comparison. Compared with the two reference patterns, the resulting composites is a mixture of BT and ST phase without any other impurities. Because no high-temperature annealing process, during which solid-solution may form, is involved in the preparation, the BT and ST are both single-phase nanocrystals. The sharp diffraction peaks of the composites also indicate high-crystallinity of the synthesized ST NWs, which is in agreement with the HRTEM analysis.[23] The surface morphology of BT/ST compounds is also shown in Fig. 2 (b), in which BT NPs are homogenously distributed in the branches-like network formed by ST NWs. Fig. 2 (c) illustrates the preparation process of BT/ST

affinity.[22,24,25] The XPS spectra are presented to verify the surface binding affinity between BT NPs and ST NWs, as well as the chelation of Sr- ions and tannic acid. As can be seen from Fig. S1, the general spectrum of BT/SrT (BT/SrT=2/1) compounds displays obvious peaks of Sr 3d and Sr 3p, which are consistent with the XRD and HRTEM analysis. It should be noted that the C 1s spectra in (b) and (c), curved into three peaks at 284.2eV, 285.5eV and 288.1eV, are attributed to the C-C, C-O and O-C=O groups from TA respectively.[26,27] Therefore, the stability of TA groups verifies the binding of shells and indicates that hydrothermal treatment does not destroy the coordination between TA and Sr-. This also indicates that by using the strong affinity of ligands, controllable growth of NWs can be realized facilely.

Fig. 3 displays the TGA and DSC curves of pure P(VDF-HFP) and 7.5 vol% nanocomposites with BT/ST fillers of different molar ratios. In Fig. 3 (a), all nanocomposites show a same stage of large weight loss near 400 °C as pure P(VDF-HFP), corresponding to the decomposition of the polymer matrix. Moreover, all the nanocomposites exhibit a single weight loss stage, indicating no impurities were introduced during the functionalization and the synthesized NWs were thermal stabilized just like the BT NPs. DSC curves obtained after erasing the thermal history are presented in Fig. 3 (b) to further confirm the impact of fillers on the polymer matrix. As can be seen, nanocomposites filled with pure ST NWs display relatively higher crystallization temperature (T_c) compared with BT NPs, both higher than that of pure P(VDF-HFP). Also, for the BT/ST nanocomposites, peaks of T_c shift to higher temperatures, indicating a hysteresis of decomposition process.[28,29] For instance, introduction of BT/ST compounds can increase T_c by about 1.7 °C, from 154.16 °C in pure P(VDF-HFP) to 155.97 °C when BT/ST=2/1. Since samples

present similar decomposition patterns to pure P(VDF-HFP) and display a hysteresis of degradation, the nanocomposites actually achieve higher thermal stability without disrupting the decomposition process of polymer matrix. Two mechanisms are
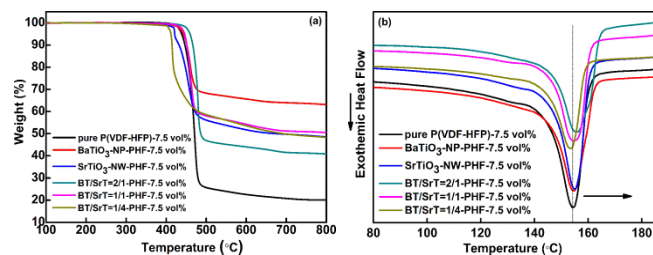

Fig. 3 Thermal analysis of pure P(VDF-HFP) and 7.5 vol% nanocomposites with BT/ST fillers of different molar ratio (a) TGA (b) DSC

responsible for the thermal stability improvement indicated in the DSC curves: On one hand, inclusion of ceramic fillers can act as a nucleating agent to promote the crystallization process of polymer matrix without changing its structure;[13,30] meanwhile, it can also curb the recrystallization and afford size reduction of domains in the polymer matrix.[14] One the other hand, NWs adhered tightly to surface can help the homogenous distribution of BT NPs in polymer matrix, leading to higher thermal stability. To explore the possible interaction between ceramics and polymer matrix, the FT-IR spectra of the nanocomposites are also illustrated in Fig. S2. The adsorption bands at 761 cm^{-1}, 794 cm^{-1} and 975 cm^{-1} correspond to the α phase while peaks at 840 cm^{-1} and 872 cm^{-1} represent the β phase of P(VDF-HFP). Specifically, the five peaks (from left to right) can be ascribed to the CH_2 rocking vibration, CF_3 stretching vibration, combined CH_2 rocking and CF_2 asymmetric stretching vibrations, combined CF_2 and C-C symmetric stretching vibrations and nonpolar trans-gauche-trans-gauche conformation respectively.[9,31,32] Because all samples exhibit the characteristic adsorption bands of pure P(VDF-HFP), the IR spectra, combined with the thermal analysis shown in Fig. 3, indicate that introduction of ceramic fillers does not change the crystalline phases and conformational modes of polymer matrix.

The freeze-fractured cross sections of BT NPs filled and BT/ST compounds filled nanocomposites are characterized by SEM in Fig. 4. As can be seen, BT NPs are embedded in the P(VDF-HFP) matrix, however, NPs tend to agglomerate and the formed cracks propagate inside the matrix. Also, the pores inside the film illustrate weak bonding between particles and polymer matrix. In Fig. 4(b), the BT/ST-PVDF film contains almost no voids between the fillers and matrix, and ST NWs dispersed homogenously in the matrix to form a river pattern. In addition, the inset micrograph shows a regular thickness of 46.5 μm over an entire range of the film. The results indicate the synthesized BT/ST compounds could form strong interfacial adhesion with P(VDF-HFP), and the prepared films are uniform, both key factors in deciding the dielectric properties of nanocomposites.[33]

Similar to many other reports, the prepared BT/ST-P(VDF-HFP) nanocomposites here can possess increased dielectric constant without obvious electrical conductivity increase as a fraction of filler volume fraction (see Fig. S3). However, the slight increase of dielectric loss, the high mass density and reduced mechanical flexibility are all typical concerns for high-
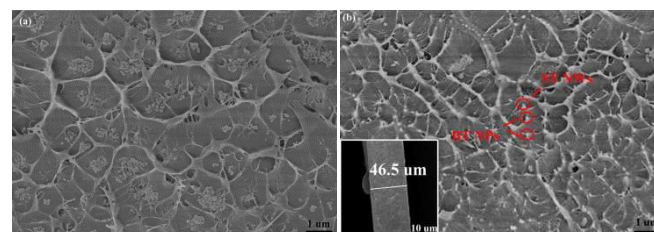

Fig. 4 SEM images of the cross-sectional of films (a) BT NPs filled (b) BT/ST (BT/ST=1/1) filled Inset: typical film thickness

performance nanocomposites.[8] For this reason, samples with 7.5 vol% are investigated in present work.The frequency dependence of dielectric parameters (dielectric constant, loss tangent and electrical conductivity) of the nanocomposites at 25 °C is shown in Fig. 5. In Fig. 5 (a), all nanocompistes filled with BT/ST can obtain higher dielectric constant than that filled with BT NPs or ST NWs, and the dielectric constant rises with the ST content increasing. This increase can be explained by the introduction of high dielectric constant ceramic crystals, which are responsible for accumulation of virtual charges at the interfaces.[34] And NWs commonly exhibit higher dielectric constant than NPs due to their large aspect ratio, as indicated by the samples filled with ST NWs and BT NPs. Due to the frequency dispersion of the P(VDF-HFP) matrix, slight dielectric constant decline is observed in all composites when frequency is over 1 MHz, while the sample of BT/ST=1/4 exhibits a larger decrease at high frequency, and this decline can be attributed to the thermal instability above.[35] It is known that the dielectric properties of nanocomposites are closely related to Maxwell-Wagner-Sillars (MWS) interfacial polarization, and the MWS polarization in the BT/ST-P(VDF-HFP) may include $MWS_{P(VDF-HFP)}$, $MWS_{BT\ NPs-P(VDF-HFP)}$ and $MWS_{ST\ NWs-P(VDF-HFP)}$.[13] MWS interfacial polarization mainly makes contributions at low-frequency range due to their long relaxation time and ST NWs can exhibit larger dielectric relaxation than BT NPs at high-frequency range.[36,37] The results indicate that excess ST NWs may worsen the dielectric properties since a large proportion of the NWs cannot be integrated onto the NPs and thus distributed randomly, causing inhomogeneous interfacial polarization in matrix. For the dielectric loss tangent in Fig. 5 (b), all but one nanocomposites remain a low loss at 1 kHz, and sample of BT/ST=2/1 exhibits a dielectric loss decline of 0.015 at 1 kHz compared with BT-P(VDF-HFP). Fig. 5 (c) also shows the frequency dependence of electrical conductivity for the nanocomposites in which the conductivity of all samples accelerates linearly with the frequency increasing. Further, those of the nanocomposites are only slightly higher than that of the pure P(VDF-HFP), indicating electron transport can be prevented by the insulating

polymer matrix.[38] As dielectric loss is mainly determined by electrical conduction and dipolar polarization at frequencies over 1 kHz, the low dielectric loss in nanocomposites can be attributed to the highly restricted polymer chain motion.[39] The stability and low value of conductivity further verify the homogenous distribution of the NPs in the PVDF matrix.[40]
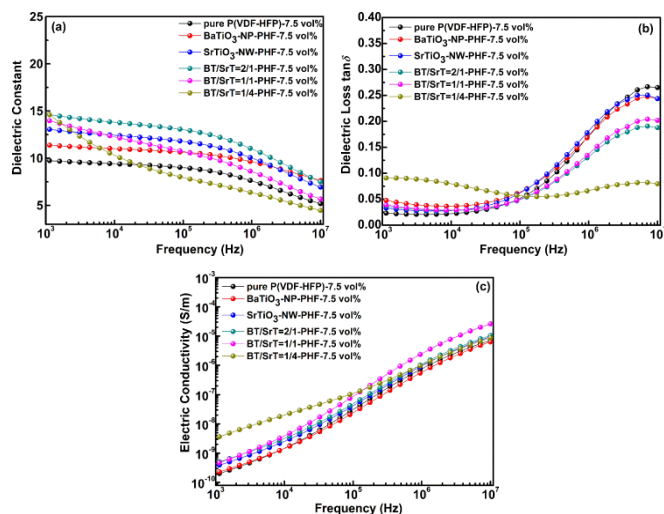

Fig. 5 Frequency dependence of dielectric parameters of pure P(VDF-HFP) and 7.5 vol % nanocomposites with BT/ST fillers of different molar ratio measured at 25 °C (a) dielectric constant (b) dielectric loss tangent (c) electrical conductivity
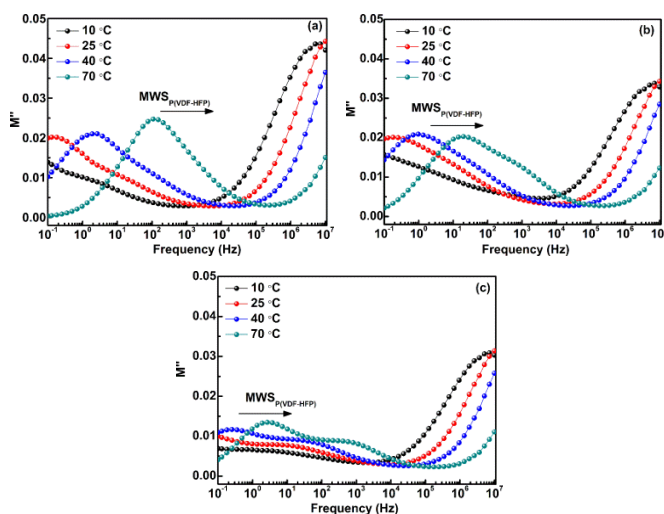

Fig. 6 Frequency dependence of electrical modulus (M'') of pure P(VDF-HFP), BT-P(VDF-HFP) and BT/ST-P(VDF-HFP) nanocomposites (BT/ST=2/1) measured at different temperatures

To further evaluate the effect of ceramic filler on the relaxation behaviour of polymer matrix, the frequency dependence of electrical modulus (*M''*) for pure P(VDF-HFP), BT-P(VDF-HFP) and BT/ST-P(VDF-HFP) nanocomposites (BT/ST=2/1) are also presented in Fig. 6. Obviously, all three samples display the same $MWS_{P(VDF-HFP)}$ polarization, which originates from the charge accumulation in the boundary between lamellar crystal and interlamellar amorphous regions. Also, the peaks shift to high frequency as the temperatures increases in all samples, which are typical characteristics of MWS

polarization.[41] Compared with pure P(VDF-HFP) and BT-P(VDF-HFP), the relaxation intensity of $MWS_{P(VDF-HFP)}$ polarization in BT/ST-P(VDF-HFP) composites is much lower, indicating the introduction of ST NWs can suppresses the space charge accumulation in the polymer matrix. The results are in
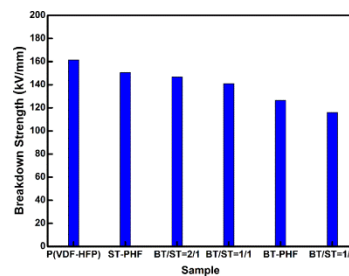
Fig. 7 Electric breakdown strength of different nanocomposites measured at room temperature
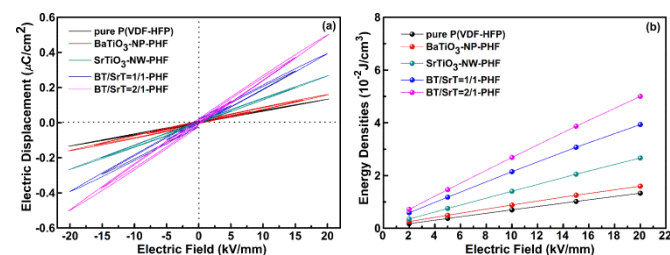
Fig. 8 Electric displacement (a) and corresponding energy storage densities (b) of the nanocomposites measured at different applied electric fields

consistent with the low conductivity of nanocomposites mentioned in Fig. 5.

Electric breakdown strength (BDS) is also an important factor in determining the possible maximum operation electric field and energy densities of the nanocomposites, which is shown in Fig. 7. It should be mentioned that all composites exhibit lower BDS values compared with pure P(VDF-HFP), since the electrical property differences between the fillers and the polymer matrix could lead to inhomogeneous distribution of electric fields near the charged interfaces.[28,42] However, despite some decrease of BDS in those modified composites, it is noticeable that the composites filled with ST NWs have higher BDS than that only filled with BT NPs. Samples with appropriate ST NWs (BT/ST=2/1 and BT/ST=1/1) can stand a high electric field over 140 kV/mm, indicating great potential for energy storage applications. It is implied that NWs filled nanocomposites are equipped with higher BDS because the NWs, with much larger aspect ratio, can cause redistribution of local electric field, leading to incomplete breakdown of the composites.[35,43] Besides the intrinsic benefits of NWs, strong interfacial adhesion between the ceramic fillers and the matrix also contributes to the enhancement of BDS when the outside electric fields are applied vertical to the in-plane directions of NWs.[44] This may partly explain the slight decline of BDS when the BT/ST=1/4.

For high dielectric constant materials, one of the expected applications is to be energy storage devices.[45] Since polarization is not linearly relied on the applied electric field for

ferroelectric materials, the energy storage density of the nanocomposites could be calculated from the electric displacement-electric field($D-E$) curves based on the following equation: Ue=∫ E dD, in which E is the electric field and D is the electric displacement.[46] In order to evaluate the energy storage abilities, Fig. 8 (a) presents the electric displacement of the nanocomposites (all in 7.5 vol%) measured at different applied electric fields with a frequency of 100 Hz. Under the same electric field, the nanocomposites can exhibit higher electric displacement compared with pure P(VDF-HFP) and incorporation of small amount of ST NWs could further increase the electric displacement obviously. The corresponding discharged energy densities as a function of applied field, calculated from the unipolar $D-E$ loops, are also shown in Fig. 7 (b). In consistent with the electric displacement, introduction of ST NWs can enhance the energy densities. For instance, when the ratio of BT/ST is 2, the electric displacement at 20 kV/mm could reach 5×10^{-2} J/cm^3, four times more than that of pure P(VDF-HFP). Because high remnant polarization can decline the discharged energy capacities of nanocomposites, this increase of energy densities is presumably due to the suppression of the MWS polarization in the nanocomposites as indicated in Fig. 6, and the reduction of the interfacial effect.[30,47,48] Therefore, it is plausible to conclude that the prepared nanocomposites could achieve larger energy densities at higher electric fields.

Conclusions

In summary, SrTiO$_3$ NWs were grafted onto the surface of BaTiO$_3$ NPs via a hydrothermal method and P(VDF-HFP)-based nanocomposites with hybrid BT/ST nanocrystals as fillers have been prepared. Thermal and microstructural analysis show that introduction of ceramics does not disrupt the crystallization process of polymer matrix, while as-synthesized BT/ST-P(VDF-HFP) nanocomposites are equipped with higher thermal stability than pure P(VDF-HFP). The dielectric measurements indicate that BT/ST-P(VDF-HFP) composites could exhibit superior dielectric properties compared with both pure P(VDF-HFP) and BT-P(VDF-HFP) composites. Despite a slight decrease of the breakdown strength after introduction of ceramics, the BT/ST-P(VDF-HFP) nanocomposites can still withstand a high electric field over 140 kV/mm. Moreover, compared with pure P(VDF-HFP), the modified nanocomposites exhibit much higher ferroelectric displacement and energy-storage densities under the same electric field. The optimal comprehensive properties are obtained when the BT/ST=2/1.The work can provide a feasible strategy of preparing high-performance nanocomposites for electrical and electronic applications.

Acknowledgements

Notes and references

[a] College of Materials Science and Engineering, Zhejiang University, Hangzhou 310027, China
[b] Zhejiang California International NanoSystems Institute, Zhejiang University, Hangzhou 310058, China
* Corresponding author. E-mail: mse237@zju.edu.cn

1 J. Chon, S. Ye, K. J. Cha, S. C. Lee, Y. S. Koo, J. H. Jung and Y. K. Kwon, *Chem. Mater.*, 2010, **22**, 5445-5452.

2. H. A. Ávila, L. A. Ramajo, M. S. Góes, M. M. Reboredo, M. S. Castro and R. Parra, *ACS Appl. Mater. Interfaces*, 2013, **5**, 505-510.

3 H. Tang, Y. Lin and H. A. Sodano, *Adv. Energy Mater.*, 2013, **3**, 451-456.

4 N. Guo, S. A. DiBenedetto, D. K. Kwon, L. Wang, M. T. Russell, M. T. Lanagan, A. Facchetti, T. J. Marks, *J. Am. Chem. Soc.*, 2007, **129**, 766-767.

5 Z. Li, L. A. Fredin, P. Tewari, S. A. DiBenedetto, M. T. Lanagan, M. A. Ratner and T. J. Marks, *Chem. Mater.*, 2010, **22**, 5154-5164.

6 J. L Vivero-Escoto, Y. D. Chiang, K. C.-W. Wu and Y. Yamauchi, *Sci. Technol. Adv. Mater.*, 2012, **13**, 013003.

7 Z. M. Dang, J. K. Yuan, S. H. Yao and R. J. Liao, *Adv. Mater.*, 2013, **25**, 6334-6365.

8 P. Kim, N. M. Doss, J. P. Tillotson, P. J. Hotchkiss, M. J. Pan, S. R. Marder, J. Y. Li, J. P. Calame and J. W. Perry, *ACS Nano*, 2009, **9**, 2581-2592.

9 M. Zhu, X. Y. Huang, K. Yang, X. Zhai, J. L. He and P. K. Jiang, *ACS Appl. Mater. Interfaces*, 2014, **6**, 19644-19654.

10 X. Y. Huang and P. K. Jiang, *Adv. Mater.* 2015, **27**, 546-554.

11 L. Y. Xie, X. Y. Huang, C. Wu and P. K. Jiang, *J. Mater. Chem.*, 2011, **21**, 5897-5906.

12 Z. M. Dang, J. K. Yuan, J. W. Zha, T. Zhou, S. T. Li and G. H. Hu, *Progress in Materials Science*, 2012, **57**, 660-723.

13 S. H. Liu, J. W. Zhai, J. W. Wang, S. X. Xue and W. Q. Zhang, *ACS Appl. Mater. Interfaces*, 2014, **6**, 1533-1540.

14 J. J. Li, S. II Seok, B. J. Chu, F. Dogan, Q. M. Zhang and Q. Wang, *Adv Mater.*, 2009, **21**, 217-221.

15 H. X. Tang and H. A. Sodano, *Appl Phys Lett.*, 2013, **102**, 063901.

16 H. X. Tang and H. A. Sodano, *Nano Lett.*, 2013, **13**, 1373-1379.

17 N. Suzuki, M. B. Zakaria, N. L. Torad, K. C.-W. Wu, Y. Nemoto, M. Imura, M. Osada and Y. Yamauchi, *Chem. Eur. J.*, 2013, **19**, 4446-4450.

18 C. C. Wang, C. M. Lei, G. J. Wang, X. H. Sun, T. Li, S. G. Huang, H. Wang and Y. D. Li, *J. Appl. Phys.*, 2013, **113**, 094103.

19 T. P. Cao, Y. J. Li, C. H. Wang, C. L. Shao and Y. C. Liu, *Langmuir*, 2011, **27**, 2946-2952.

20 Y. Song, Y. Shen, H. Y. Liu, Y. H. Lin, M. Li and C. W. Nan, *J. Mater. Chem.*, 2012, **22**, 8063-8068.

21 H. X. Tang, Z. Zhou and H. A. Sodano, *ACS Appl. Mater. Interfaces*, 2014, **6**, 5450-5455.

22 T. Zeng, X. L. Zhang, Y. Y. Guo, H. Y. Ni and Y. Q. Cai, *J. Mater. Chem. A*, 2014, **2**, 14807-14811.

23 Y. J. Liu, G. Stefani, J. Rathousky, O. Hayden, T. Bein and D. F. Rohlfing, *Chem. Sci.*, 2012, **3**, 2367-2374.

24 Q. Ye, F. Zhou and W. M. Liu, *Chem. Soc. Rev.*, 2011, **40**, 4244-4258.

25 L. X. Chen, T. L, M. C. Thurnauer, R. Csencsits and T. Rajh, *J. Phys. Chem. B*, 2002, **106**, 8539-8546.

26 Y. D. Lei, Z. H. Tang, R. J. Liao and B. C. Guo, *Green Chem.*, 2011, **13**, 1655-1658.

27 Y. Zhang, Y. L. Su, J. M. Peng, X. T. Zhao, J. Z. Liu, J. J. Zhao and Z. Y. Jiang, *Journal of Membrane Science*, 2013, **429**, 235-242.

28 K. Yang, X. Y. Huang, Y. H. Huang, L. Y. Xie and P. K. Jiang, *Chem. Mater.*, 2013, **25**, 2327-2338.

29 L. Gao, J. L. He, J. Hu and Y. Li, *J. Phys. Chem. C*, 2014, **118**, 831-838.

30 J. H. Jin, S. S. Yang amd B. S. Bae, *Polym. Chem.*, 2011, **2**, 168-174.

31 W. Wu, X. Y. Huang, S. T. Li, P. K. Jiang and T. Toshikatsu, *J. Phys. Chem. C*, 2012, **116**, 24887-24895.

32 Shalu, S. K. Chaurasia, R. K. Singh and S. Chandra, *J. Phys. Chem. B*, 2013, **117**, 897-906.

33 Q. G. Chi, J. Sun, C. H. Zhang, G. Liu, J. Q. Lin, Y. N. Wang, X. Wang and Q. Q. Lei, *J. Mater. Chem. C*, 2014, **2**, 172-177.

34 M. Rahimabady, M. S. Mirshekarloo, K. Yao and L. Lu, *Phys. Chem. Chem. Phys.*, 2013, **15**, 16242-16248.

35 P. H. Hu, Y. Shen, Y. H. Guan, X. H. Zhan, Y. H. Li, Q. M. Zhang and C. W. Nan, *Adv. Funct. Mater.*, 2014, **24**, 3172-3178.

36 L. Y. Xie, X. Y. Huang, Y. H. Huang, K. Yang and P. K. Jiang, *ACS Appl. Mater. Interfaces*, 2013, **5**, 1747-1756.

37 Z. M. Dang, H. Y. Wang and H. P. Xu, *Appl Phys Lett.*, 2006, **89**, 112902.

38 N. Suzuki, Y. Kamachi, Y. D. Chiang, K. C.-W. Wu, S. Ishihara, K. Sato, N. Fukata, M. Matsuura, K. Maekawa, H. Tanabe, K. Ariga and Y. Yamauchi, *CrystEngComm*, 2013, **15**, 4404-4407.

39 T. C. Wang, H. H. Li, F. Wang, J. M. Schultz and S. Yan, *Polym. Chem.*, 2011, **2**, 1688-1698.

40 K. Brandt, C. Neusel, S. Behr and G. A. Schneider, *J. Mater. Chem. C*, 2013, **1**, 3129-3137.

41 L. Y. Xie, X. Y. Huang, B. W. Li, C. Y. Zhi, T. Tanaka and P. K. Jiang, *Phys. Chem. Chem. Phys.*, 2013, **15**, 17560-17569.

42 F. He, S. T. Lau, H. L. Chan and J. T. Fan, *J. Adv. Mater.*, 2009, **21**, 710-715.

43 V. Thavasi, G. Singh and S. Ramakrishna, *Energy Environ. Sci.*, 2008, **1**, 205-221.

44 P. H. Hu, Y. Song, H. Y. Liu, Y. Shen, Y. H. Lin and C. W. Nan, *J. Mater. Chem. A*, 2013, **1**, 1688-1693.

45 S. B. Luo, S. H. Yu, R. Sun and C. P. Wong, *ACS Appl. Mater. Interfaces*, 2014, **6**, 176-182.

46 K. Yu, Y. J. Niu, Y. Y. Bai, Y. C. Zhou and H. Wang, *Appl. Phys. Lett.*, 2013, **102**, 102903.

47 Y. Song, Y. Shen, H. Y. Liu, Y. H. Lin, M. Li and C. W. Nan, *J. Mater. Chem.*, 2012, **22**, 16491-16498.

48 B. J. Chu, M. R. Lin, B. Neese, X. Zhou, Q. Chen and Q. M. Zhang, *Appl. Phys. Lett.*, 2007, **91**, 122909.

Journal of Materials Chemistry C Accepted Manuscript
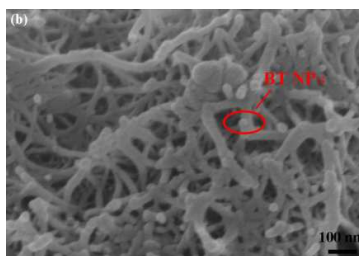
Highlights

SrTiO$_3$ nanowires were hydrothermally grafted onto BaTiO$_3$ nanoparticles and BaTiO$_3$/SrTiO$_3$-P(VDF-HFP) composites exhibited enhanced dielectric properties.